## COMMUNICATION

Check for updates

# Unraveling energetics and states of adsorbing oxygen species with MoS$_2$ for modulated work function†

Hejin Yan, Hongfei Chen, Xiangyue Cui, Qiye Guan, Bowen Wang and Yongqing Cai [ID] *

MoS$_2$ and related transition metal dichalcogenides (TMDs) have recently been reported as having extensive applications in nanoelectronics and catalysis because of their unique physical and chemical properties. However, one practical challenge for MoS$_2$-based applications arises from the easiness of oxygen contamination, which is likely to degrade performance. To this end, understanding the states and related energetics of adsorbed oxygen is critical. Herein, we identify various states of oxygen species adsorbed on the MoS$_2$ surface with first-principles calculations. We reveal a "dissociative" mechanism through which a physisorbed oxygen molecule trapped at a sulfur vacancy can split into two chemisorbed oxygen atoms, namely a top-anchoring oxygen and a substituting oxygen, both of which show no adsorbate induced states in the bandgap. The electron and hole masses show an asymmetric effect in response to oxygen species with the hole mass being more sensitive to oxygen content due to a strong hybridization of oxygen states in the valence band edge of MoS$_2$. Alteration of oxygen content allows modulation of the work function up to 0.5 eV, enabling reduced Schottky barriers in MoS$_2$/metal contact. These results show that oxygen doping on MoS$_2$ is a promising method for sulfur vacancy healing, carrier mass controlling, contact resistance reduction, and anchoring of surface electron dopants. Our study suggests that tuning the chemical composition of oxygen is viable for modulating the electronic properties of MoS$_2$ and likely other chalcogen-incorporated TMDs, which offers promise for new optoelectronic applications.

## New concepts

MoS$_2$ has been extensively explored for integration into advanced electronics and is leading the trend of next-generation semiconductor devices. However, the low formation energy of sulfur vacancies leads to intrinsic n-type doping character and degrades the original material performance. Furthermore, the existence of ubiquitous oxygen species, likely to be introduced during manufacturing, processing, or ambient exposure, emphasizes the need for investigation of the atomic-scale mechanism of oxygen doping. Here, we discover a "dissociative" mechanism of molecular oxygen trapped at sulfur vacancies to facilitate single-atomic oxygen doping in MoS$_2$, setting the foundation for forming molybdenum oxy-sulfide. Density-functional theory calculations show that there exist two favorable states of single-atomic oxygen: the top stacking and bottom substituting states. Interestingly, the oxygen doping induces a lattice strain field which competes with the stoichiometry to tune the carrier mass. Furthermore, we demonstrate modulation of the work function and accordingly the Schottky barrier in MoS$_2$/metal contact with varying oxygen concentrations. This sets the foundation of oxygen doping engineering of MoS$_2$ for sulfur vacancy healing, contact resistance reduction, and anchoring of surface electron dopants for a plethora of applications.

## Introduction

Molybdenum disulfide (MoS$_2$), an emerging two-dimensional (2D) material consisting of a Mo monolayer sandwiched between two S monolayers, has recently attracted extensive

*Joint Key Laboratory of the Ministry of Education, Institute of Applied Physics and Materials Engineering, University of Macau, Taipa, Macau, China.*
*E-mail: yongqingcai@um.edu.mo*

attention due to its high mechanical flexibility and intriguing electronic properties.[1–3] Monolayer and few-layer MoS$_2$ are being intensively explored for field effect transistors,[4,5] sensors,[6,7] photocatalysis,[8] energy harvesting,[9–11] and other advanced optoelectronics.[12–14] Extraordinary performance was obtained by depositing MoS$_2$ on high-dielectric oxides leading to carrier mobility up to 200 cm$^2$ V$^{-1}$ s$^{-1}$ and a high switching ratio of $\sim 10^8$, making it a substitute for classical silicon semiconductors for miniaturization.[15]

Thus far, extension of Moore's law by continually scaling down silicon-based integrated circuits has encountered a dilemma.[16] As a 2D alternative, MoS$_2$ is a promising material for balancing device minimization and performance optimization.[17] Its atomic level thickness and moderate carrier mobility are favorable for gate controllability.[18,19] Nevertheless, the semiconducting character and weak dielectric screening make monolayer MoS$_2$ extremely sensitive to intrinsic defects, extrinsic adsorbates, and strain. Indeed, as the most common natural defect, sulfur vacancy (V$_S$),

at a typical defect density of $10^{13}$ cm$^{-2}$, degrades carrier mobility due to defective bandgap states and lifting of Schottky barriers through Fermi-level pinning.[20,21]

Owing to their atomically thin character and high surface-to-volume ratio, MoS$_2$ nanostructures are subjected to environmental doping by molecular adsorbates which has a pronounced effect on their electronic and optoelectronic properties.[22,23] On the other hand, it has been widely recognized that molecular adsorbate doping is an effective technique for defect passivation in 2D electronics.[24,25] Among various possible adsorbates, oxygen species must be the most prevalent impurity source after or during growth of 2D materials. Unintentional uptake of O species in a MoS$_2$ layer may arise from (1) synthesis due to incomplete sulfurization of MoO$_3$ or the presence of oxygen using chemical vapor deposition;[26–30] (2) introducing oxide substrates, normally Al$_2$O$_3$ or SiO$_2$, and high-dielectric capping layers like HfO$_2$ or ZrO$_2$ during device integration, where oxygen vacancies in the oxides, generated by gate voltage or temperature gradient, can be formed and the depleted O atoms are susceptible to recapture by the MoS$_2$ layer;[31–34] (3) exposing MoS$_2$ layers to atmospheric adsorbates in ambient conditions during application.[35] Other processes with a high possibility of introducing O impurities include adopting an ionic-liquid gate, liquid-phase exfoliation, plasma-assisted nano-printing, and synthesizing MoS$_2$-based nanohybrids.[36–40] Compared with a perfect surface, the adhesion and effect of O species should be more prominent if the layer is partially reduced by forming V$_S$ in the basal plane or dissected for ribbons or nanoflakes due to abundant dangling bonds. In contrast to the well-understood effects of O on graphene (bandgap opening and formation of graphene oxide) and boron nitride (BN), a clear picture of O species evolution in MoS$_2$ is still absent; to be specific, the energetics and kinetics of O species and the impact of adsorbed O species on structural modification and electronic properties of MoS$_2$ are still unclear,[41,42] although their pronounced effects on healing of vacancy sites and reducing the MoS$_2$/metal contact barrier have been recognized.[43,44]

In this work, we present a theoretical investigation of the surface affinity of MoS$_2$ toward O species based on a first-principles study. We identify the possible adsorbing states and types of oxygen atoms on MoS$_2$. A dissociative mechanism of molecular oxygen adsorbing at a V$_S$ into two atomic species, a substituting oxygen and a top oxygen, is revealed. We demonstrate substantial atomic displacements and gradient strains surrounding each single oxygen dopant. Through the uptake of more oxygen atoms, lattice strain is developed and scaled with the oxygen content. We show an opposite effect on electron and hole mass with this chemical functionalization, but the electron mass is less sensitive to the oxygen content than the hole
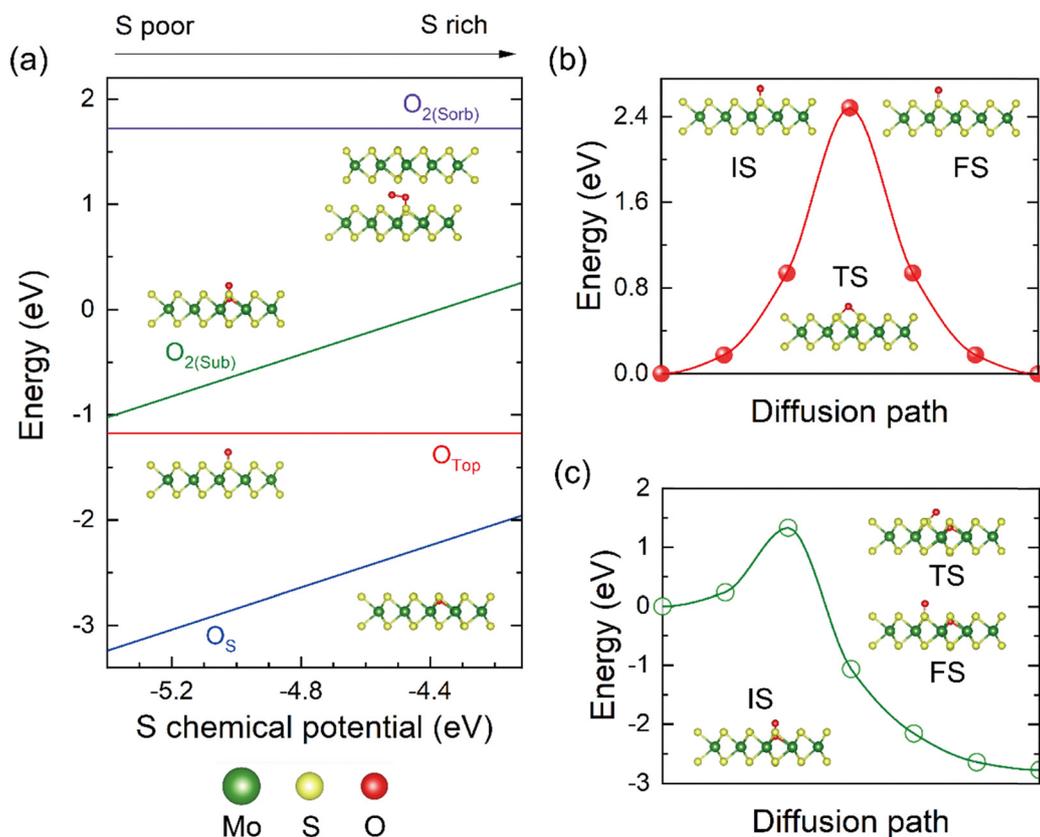


Fig. 1 (a) Sulfur chemical potential ($\mu_s$) determined the formation energy for various O adsorbates on MoS$_2$. The $\mu_s$ in the S-rich condition is equal to that in the S$_8$ molecular crystal, and in the extreme S-poor limit $\mu_s$ is bounded by the formation of Mo in the film. (b) Activation energy for O$_{Top}$ diffusing above the MoS$_2$ layer. (c) Activation energy for O$_{2(Sub)}$ decomposing into a (O$_{Top}$, O$_S$) pair. The green, yellow, and red spheres represent Mo, S, and O atoms, respectively. The insets in (b) and (c) are the structure of the initial state (IS), transition state (TS), and final state (FS).

# Results and discussion

### Energetics, dynamics and states of adsorbed oxygen species

In the graphene case, more than one type of oxygen species is involved in modifying the properties.[45] Here, energetics and stability of O species on a $MoS_2$ monolayer are quantitatively evaluated by considering the following potential adsorption configurations (Fig. 1(a)): oxygen adsorption above the anionic plane sitting atop a S atom ($O_{Top}$), oxygen atom substituting a S atom ($O_S$) which is equivalent to the oxygen atom occupying the S vacancy, and molecular $O_2$ substituting a S atom which is equivalent to formation of peroxide species or oxygen molecule trapped by a S vacancy ($O_{2(Sub)}$). Other possible adsorptions states, like O occupying above the hollow position defined by the equilateral triangle formed by three S atoms, are unstable (Fig. S1 and Table S1, ESI†). The formation energy ($E_f$) for the $O_{Top}$ is $-1.2$ eV with an O–S bond length of 1.483 Å. For the $O_S$ case, this state shows the lowest $E_f$ of $-3.25$ eV under the S-poor condition. This indicates that the substituting O species is very likely to occur in the $MoS_2$ layer, especially for films after reducible gas treatment, e.g., a hydrogen plasma increases the $V_S$ on the $MoS_2$ basal plane.[46,47] The substituting O atom relaxes about 0.412 Å toward the middle Mo layer with an O–Mo bond length of 2.052 Å. For the $O_{2(Sub)}$ structure, $E_f$ is still negative but higher than that of the $O_S$ type. The O–O bond length is elongated to 1.374 Å compared with 1.211 Å of a free $O_2$ molecule, implying a strong activation of the O–O bond by populating the $2\pi^\star$ antibonding orbital of the $O_2$ molecule.

Binding of an $O_2$ molecule above the anionic basal plane of perfect $MoS_2$ is unstable and shows very weak physisorption on the monolayer. However, for multi-layer or bulk $MoS_2$, oxygen molecules may be trapped inside the van der Waals (vdWs) gap, denoted as $O_{2(Sorb)}$. As shown in Fig. 1(a), the adsorption is an endothermic process with a positive $E_f$ of 1.7 eV. In this meta-stable configuration, one of the O atoms forms a chemical bond with a S atom in one $MoS_2$ layer, while the other is tilted toward the gap above the center of a triangle formed by S atoms of the same $MoS_2$ layer. The O–O and the O–S bond lengths are 1.465 Å and 1.591 Å, respectively. Additionally, the much longer O–O bond in $O_{2(Sorb)}$ within the vdWs gap than that in $O_{2(Sub)}$ trapped at the vacancy suggests higher amounts of electrons transferring to occupy the $2\pi^\star$ antibonding orbital of the $O_2$ molecule, probably due to a denser electron density in the vdWs gap. Therefore, through thermal activation under finite temperature, we can still expect the entry and adsorption of $O_2$ molecules in bulk or multi-layer $MoS_2$ despite the ultraweak adsorption above the basal plane of the surface. Fig. 1(b) shows activation barriers calculated by the climbing image nudged elastic band (CI-NEB) method for the O species diffusing on the surface. For $O_{Top}$ species, the barrier for O jumping along the neighboring lattice is around 2.4 eV. For $O_{2(Sub)}$, there is likely to be a dissociative process via $O_{2(Sub)} \rightarrow O_{Top} + O_S$, where the

protruding O atom moves to the top of its neighboring S atom simultaneously breaking the O–O bonding and the activation energy is around 1.2 eV, much lower than that of the $O_{Top}$ species. This indicates a viable way of filling $V_S$ through molecular oxygen while forming oxygen decoration. Notably, the low-temperature preparation of $MoS_2$ below 100 °C is plagued by the increased adsorption of water, serving as an additional oxygen contamination source, and the related $H_2O$ molecule adsorption and dissociation on $MoS_2$ have been reported.[48,49] Here, the energy barriers for $O_2$ dissociation in bulk-phase $MoS_2$ are also considered (Fig. S2, ESI†). This barrier height is correlated with the stability of bulk-phase $MoS_2$, as the diffusion and dissociation of $O_2$ molecules change the interlayer vdWs interactions and promote the exfoliation of the $MoS_2$ monolayer.

### Atomic displacement and gradient strain surrounding oxygen dopants

Fig. 2(a) and (b) illustrate the relaxation of periphery S/Mo atoms around the single $O_{Top}$ and $O_S$ dopant centers in the supercell, respectively. The introduction of O species in the $MoS_2$ monolayer causes gradient strains, leading to the host lattice expansion (for $O_{Top}$) and contraction (for $O_S$). For the $O_{Top}$ species, the three nearest Mo atoms relaxed outward by about 0.029 Å. The magnitude of the strain field, indicated by the length of orange arrows, decays rapidly away from the oxygen species; for instance, the second-nearest-neighbor S atoms relax only outwardly by about 0.003 Å. For the $O_S$, there is a strong compressive field around the substituting dopant center with stronger O–Mo binding and a shorter O–Mo bond length, due to a smaller atomic radius and a lower electro-negativity of the O atom than that of the S atom. The three neighboring Mo atoms move inward 0.129 Å, and the next-nearest S species relaxed inward 0.065 Å with appreciable strain even extends to about 4 or 5 nearest neighbors. In a word, we identify a sizable strain field associated with a substitutional oxygen dopant in $MoS_2$. This is expected to be true in other 2D materials. With the lack of a continual lattice in 3D crystal, 2D materials are prone to generate a larger area of buffering region with the formation of gradient strain around the dopant.

We next examine the effect of varying the content of oxygen dopants. To simulate the ambient condition where oxygen sources largely access one surface of $MoS_2$, the other side would be blocked due to the substrate. In this extreme condition, all O atoms are modeled to adsorb on one facet of the S–Mo–S layer. As for the case of O adsorbing on both facets, all the O species are uniformly distributed with maximized separation, and the more complicated oxygen cluster formation on the surface is not considered (see Fig. S3 and S4 for the optimized structures, ESI†). Notably, the uptake of O atoms does not induce any dangling bonds, which is favorable for keeping planeness and speed of transporting carriers.[50]

Highly concentrated O-doped $MoS_2$ becomes molybdenum oxy-sulfide ($MoS_yO_x$), and here the evolution of the lattice constant of two types of molybdenum oxy-sulfide ($MoS_2O_x$ containing $O_{Top}$ and $MoS_{2-x}O_x$ containing $O_S$ with $x$ being the content of oxygen normalized to normal chemical formula)
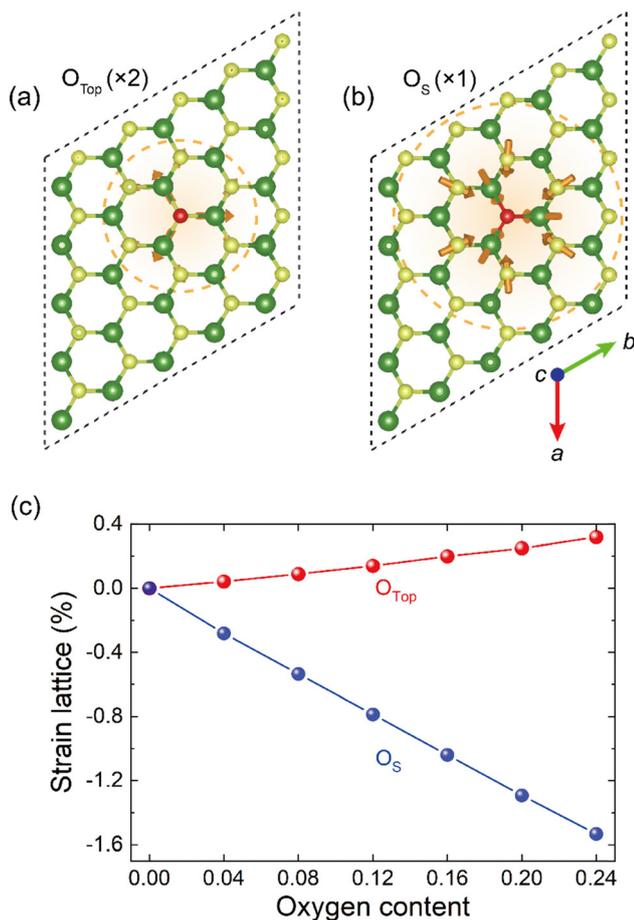
**Fig. 2** Doping-induced strain field by single $O_{Top}$ (a) and $O_S$ (b). The orange arrows denote displacements of atoms from their original positions in a pristine lattice to positions in a defective lattice, with the arrow lengths representing the magnitudes of the adjustments. For visualization purposes, the length of the displacement vectors in (a) is doubled. The dashed black line represents the simulation supercell box. (c) Lattice strain intensity (expansion for $O_{Top}$ and shrinkage for $O_S$) as a function of oxygen content. The $5 \times 5 \times 1$ supercell of molybdenum oxy-sulfide is used to account for the lattice evolution.

layer with different stoichiometry is calculated and shown in Fig. 2(c). For the $O_{Top}$ case, the lattice constant increases gradually, and the strain ($\delta$)–O content ($x$) relation scales as $\delta = C \times x$ with $C$ fitted to be 1.32, consistent with the previous expansive strain field around the dopant center shown in Fig. 2(a). For the $O_S$ case, introducing $O_S$ causes significant compressive strain on the lattice. The $\delta$–$x$ relation also follows $\delta = C \times x$ with $C$ fitted to $-6.36$, showing a much larger distortion of the $MoS_2$ host lattice than the $O_{Top}$ case. For instance, for the O content with $x$ of 0.24, the induced lattice strain is 0.3% for $O_{Top}$ and $-1.5\%$ for $O_S$. While here the results are only calculated for single-layer $MoS_2$, similar scaling behavior of the lattice constant with oxygen dopant would be true for multi-layer $MoS_2$ and for adsorption evenly at both basal planes of $MoS_2$ (Tables S2 and S3, ESI†). For the latter, due to the intercalation of O or $O_2$ species (Fig. 1) in the vdWs gap, the lattice constant normal to the atomic plane would also increase

with the O content. From an experimental perspective, Burrns *et al.* used high-resolution transmission electron microscopy (HR-TEM) to detect local strain fields induced by vacancies in $MoS_2$. They suggest that O atoms adsorbed on a vacant S site, denoted as $O_S$ in our work, lead to the lattice contraction at high irradiation fluences.[51] This phenomenon aligns with the trend in Fig. 2(b). Recently, Kumar *et al.* found the combination of tensile strain and the absence of charged oxygen adatoms, denoted as $O_{Top}$ in our work, triggering a drastic photoluminescence (PL) redshift of $\sim 130$ meV for $MoS_2$.[52] These findings suggest that surface oxygen dopants and induced lattice strain field have profound effects on modifying the electronic properties.

### Modulation of band structure, effective mass and work function

We next show the evolution of the electronic structures of $MoS_2$ after surface oxygen treatment. Fig. 3(a) shows band structures of the $O_{Top}$ and $O_S$ cases, where the contribution of O atoms is projected out and their components are scaled by the size of red circle markers at each $k$ point and band. In contrast to the bandgap opening of graphene oxide,[53] there is no strong modification of bandgap with mild O decoration. The bandgap of the oxygen-decorated $MoS_2$ monolayer decreases almost linearly with the oxygen content varying from 0.04 to 0.24 for $O_{Top}$ and $O_S$ oxygen species (Fig. 3(c)). As an iso-valent dopant, the addition of oxygen, either the substitutional $O_S$ or the top $O_{Top}$, does not induce any defective levels in the bandgap, thus trapping of carriers by these two types of O species is unlikely to be prominent. However, there is evident modification of the valence band edge through orbital hybridization, while modulation of the conduction band edge is tiny as there is negligible O hybridization with Mo atoms.

Since band edges are critically important in terms of effective mass of carriers and deformation energy of the frontier orbitals, the adsorption of O species may influence the performance of the $MoS_2$ layer such as mobility of carriers, especially for holes. Fig. 3(b) presents the partial density of states (PDOS) for $O_{Top}$, $O_S$, and $O_{2(Sub)}$. For $O_{Top}$ and $O_S$, the O states spread over the whole valence band and no defective states occur in the gap. In contrast, for $O_{2(Sub)}$ adsorption, the clamped $O_2$ at the S vacancy site induces new states above the valence top. From the plot of surface charge density of valence band maximum (VBM) and conduction band minimum (CBM) shown in Fig. S5a and c (ESI†), these O states are strongly localized, suggesting relatively weak hybridization of the molecule with the $MoS_2$ substrate. The additional peak located $\sim 0.3$ eV above the VBM corresponds to the $\pi$ orbital of surface $O_2$. According to these results, the shallow defective level would have a weak effect on carrier mobility, as $O_{2(Sub)}$ is metastable and has a tendency to transfer into the $O_{Top}$ and $O_S$ states.

Fig. 4 shows the evolution of electron/hole effective mass with the content of O species. Electron (hole) mass of pristine $MoS_2$ monolayer is 0.46 $m_e$ ($-0.60$ $m_e$), consistent with a previous report of 0.47 $m_e$ ($-0.60$ $m_e$).[54] Upon uptake of O species, for $O_{Top}$ cases (Fig. 4(a)), the magnitude of hole mass increases steadily from $-0.60$ $m_e$ for zero oxygen content to $-0.75$ $m_e$ with O content $x$ of 0.24. In contrast, the trend for the
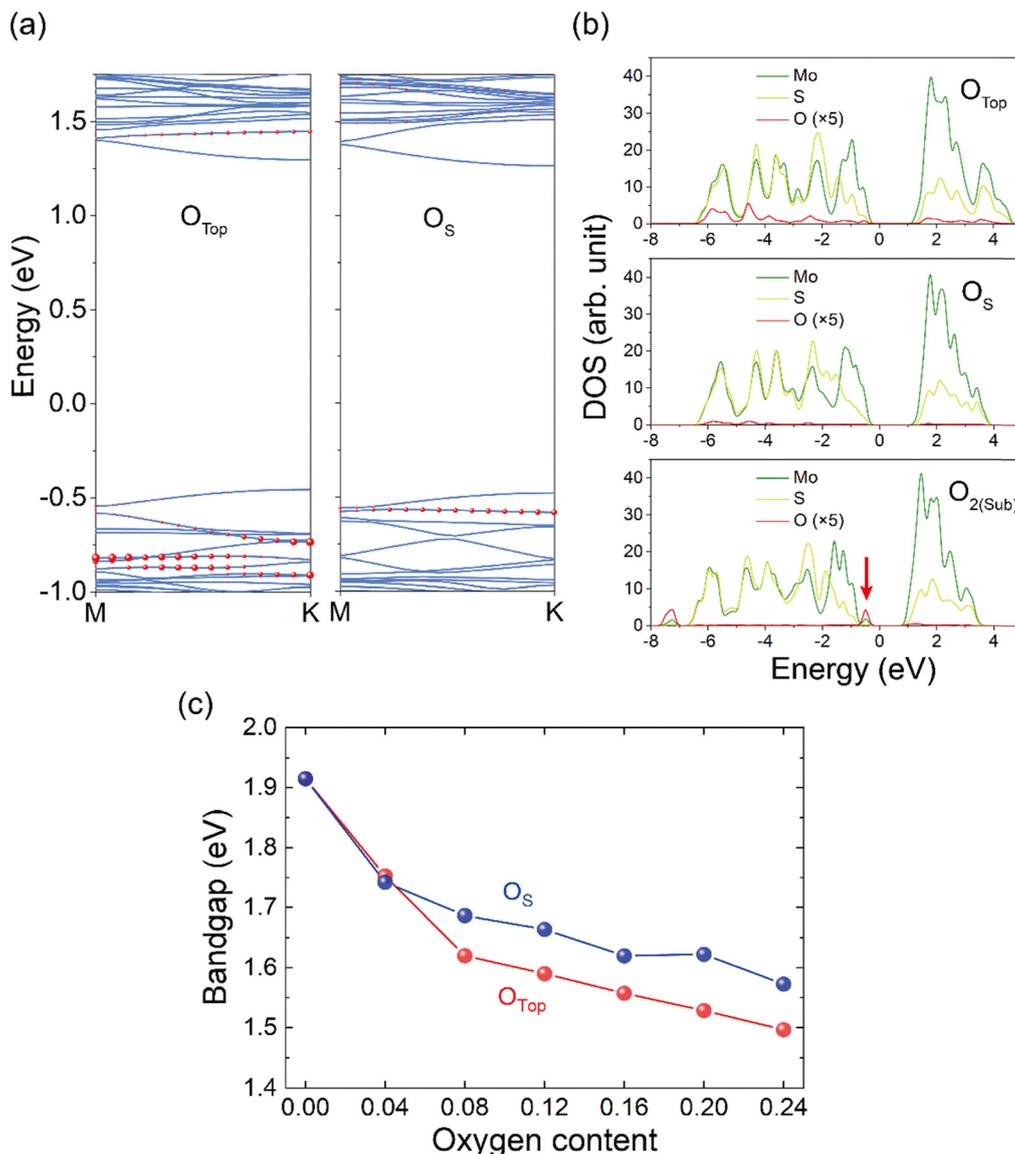
Fig. 3 Electronic structures in oxygen-decorated $MoS_2$. (a) Oxygen contribution projected band structure of $O_{Top}$ and $O_S$. The size of the red circle markers indicates the contribution from oxygen orbitals. (b) Partial density of states (PDOS) of $O_{Top}$, $O_S$, and $O_{2(Sub)}$. The red arrow denotes the in-gap states in $O_{2(Sub)}$. (c) Bandgap as a function of oxygen content.

$O_S$ case (Fig. 4(b)) starts with a plateau occurring at the onset corresponding to the dilute doping limit, the hole mass then decreases with increasing O content and levels off at $-0.22\ m_e$ at $x$ equal to $0.12\ m_e$. For both cases, the value of electron mass fluctuates around $\sim 0.50 m_e$, and the adsorption of O species has a weaker effect on electron mass than on hole mass. According to Fig. 3(a) and (b), this is due to a weaker hybridization of O states with Mo orbitals at the CBM while a strongly coupled O component at the VBM (also see Fig. S6 and S7, ESI†). Similar results also hold true for oxygen species distributing on both facets of sulfur in $MoS_2$ (Fig. S8 and S9, ESI†).

In fact, such doping-level-controlled carrier mass is a synergetic effect of chemical variation and strain modification after introduction of O species. For the $O_{Top}$ case, the adsorption only leads to a tiny strain within the range of O content

$x \leq 0.24$; thus the increasing hole mass is solely attributed to the chemical variation of the top O atoms above the S atoms. However, for $O_S$, as shown in Fig. 2(b), it induces significant strain on the host lattice. To decouple the effect of the chemical modification of O atoms from strain field and identify dominant factors affecting the carrier mass, we performed additional calculations with a frozen lattice where the lattice constant is kept the same for all the O content to exclude the strain effect. The lattice constants of the $O_{Top}$ and $O_S$ models with varied oxygen content are fixed to the same lattice values as their 0.04 oxygen content cases, respectively (see Table S2 and S3 for details, ESI†). The $x$-electron/hole mass relationship for the frozen lattice is represented by the dashed lines in Fig. 4(a) and (b). For $O_{Top}$, the lines associated with holes for the frozen lattice are nearly overlapped with those for the
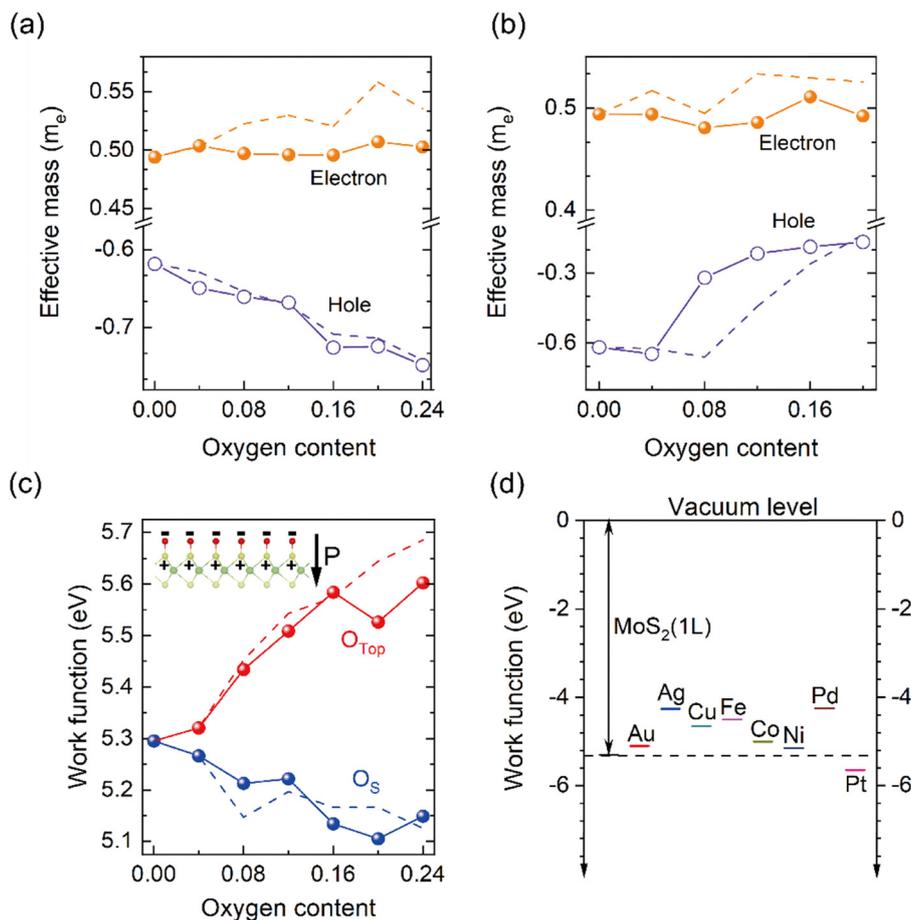
Fig. 4 Oxygen content-mediated effective mass for the single $O_{Top}$ (a) and $O_S$ (b) species. (c) Work function of $O_{Top}$ and $O_S$ as a function of oxygen content. The solid and dashed lines correspond to calculations with structures of relaxed lattice of oxygen-doped MoS$_2$ and frozen lattice of pristine MoS$_2$, respectively. The inset shows the inward surface dipole associated with surface top-type oxygen, $O_{Top}$, accounting for the increase of work function. (d) Work function alignment of monolayer MoS$_2$ and normal metal electrodes.

relaxed lattice. This is reasonable considering the moderate structural relaxation of the host layer with O uptake. For $O_S$, both trends of with/without strain are similar, showing a lighter hole mass with greater oxygen incorporation. However, there is a clear deviation of the hole mass between the relaxed and fixed cases. For $x$ between 0.08 and 0.2, the hole mass of frozen lattice is linearly correlated with $x$ indicating the substituting O decreases the hole mass (violet dashed line in Fig. 4(b)). While for the relaxed lattice, the slope of the line continually decreases, and the hole mass levels off to $-0.22m_e$ at a doping content of 0.12 (violet solide line in Fig. 4(b)). Therefore, compressive strain induced by dense $O_S$ tends to promote the hole mass.

A similar strain effect has also been found in other types of sulfide semiconductor.[55] In a word, upon introduction of O, while the chemical modification decreases the hole mass, there is a concomitant increase of hole mass due to the compressive strain, thus decreasing the slope of the $x$-hole mass profile in the relaxed lattice case. This inherent strain accompanied by the O doping would play an important role in affecting the electronic properties and accordingly carrier transport behavior in field effect transistors (FETs). Our study shows that creating

$O_S$ species with an appropriate O content may effectively decrease the hole mass thus promoting the hole mobility, whereas the electron mass is less affected. Compared with the $V_S$-induced flat defect states (Fig. S10b, ESI†) for trapping and scattering charge carriers, the adsorbed oxygen atoms somehow heal the vacancies and mitigate the defect effect on carrier mobilities. Indeed, Wei et al. fabricated oxygen-doped MoS$_2$ monolayer at the wafer scale, and the final FET device shows high mobilities with an average of 78 cm$^2$ V$^{-1}$ s$^{-1}$, being greater than that of intrinsic MoS$_2$ FETs of 48 cm$^2$ V$^{-1}$ s$^{-1}$.[56] Tang et al. also suggested that moderate oxygen doping significantly improves the carrier mobilities of MoS$_2$ by removing $V_S$.[57]

Next, we demonstrate that by controlling the type and content of O species, the work function ($W$) of the hybrid MoS$_y$O$_x$ layer can be tuned, which is highly desired for electronic devices to control band alignment with metal electrodes. Several metals have been proven to form a Schottky contact at the MoS$_2$/metal interface, and an effective strategy for reducing the Schottky barrier height (SBH) is the shifting of $W$ of MoS$_2$.[58–60] In Fig. 4(c), $W$ is calculated by subtracting the Fermi energy from the electrostatic potential in the middle of the vacuum layer (eqn (5)).[61,62] $W$ of the MoS$_y$O$_x$ layer increases

monotonically from 5.3 to 5.6 eV for $O_{Top}$ species with $x$ increasing from 0 to 0.24. In contrast, $W$ decreases gradually with increasing $O_S$ content, implying overall effective surface positive charges with the presence of $O_S$ species. The modification from 5.6 eV (for $O_{Top}$) to 5.15 eV (for $O_S$) at an O content of 0.24 indicates a large modulation space of $W$ (around 0.5 eV) with the addition and control of O species in the film. Due to the larger electronegativity of an oxygen atom than that of a sulfur atom, the oxygen is negatively charged, and the sulfur is positively charged. A dipole is induced associated with the oxygen–sulfur pair with the dipole direction pointing inwardly from the adsorbing oxygen atom to its bonded sulfur atom (see the inset in Fig. 4(c)). On the $O_{Top}$ surface, the exterior negatively charged oxygen inhibits electrons escaping from the surface and promotes $W$. While for the $O_S$ surface, the reversed dipole direction is favorable for surface electron escape, hence reducing $W$. Fig. 4(d) shows the comparison and alignment of $W$ of pristine $MoS_2$ monolayer and common metal electrodes. By considering the variance of $W$ induced by different types and varying content of oxygen as shown in Fig. 4(c), Au, Co, Ni, and Pt are predicted to be suitable for contact with the $MoS_yO_x$ layer due to a low SBH. For comparison, Gupta *et al.* used Kelvin probe force microscopy (KPFM) to measure $W$ of $MoS_2$, for which the existence of $MoO_{3-x}$ phase alters $W$ from 4.98 to 5.56 eV.[63] In fact, such dopant-controlled electronic structures were also observed in other TMDs. Oberoi *et al.* adopted a self-limiting oxidation method to convert a top-layer $WSe_2$ channel to $WO_xSe_y$ alloy, achieving high-performance p-type FETs with a 5-fold improvement in the on-state performance and a 9-fold reduction in the contact resistance.[64]

Due to the relatively wide bandgap of $MoS_2$ and thus an enlarged SBH, the contact resistance of the $MoS_2$/metal junction is supposed to be much larger than that of the graphene/metal junction.[65] A variable $W$ of the $MoS_2$ layer is highly important for tuning the SBH. The demonstrated tunable range of $W$ of $\sim 0.5$ eV by O doping is large compared to the intrinsic bandgap of the monolayer (1.8 eV). Therefore, surface modification can significantly modulate the barrier of carrier injection at a metal/$MoS_2$ contact and may even allow control of carrier polarity in the film by tuning the content and the type of O species in the monolayer. For silicon or other oxide as the channel material, the energetic alignment at the interface can be controlled by dopants or defects.[66] However, unlike graphene, the presence of a finite gap of $MoS_2$ may create in-gap states upon doping which will trap the charges and affect the carrier mobility. Here we prove that the introduction of iso-chemical species like substituting O, being free of in-gap levels, is highly important for tuning the properties of $MoS_2$ for various applications. The strain-chemical–property relationships inherent in the O modification can be tuned by controlling the adsorbing states of O species on the $MoS_2$ monolayer, enabling a synergetic effect of strain and chemical functionalization. Moreover, due to the more electronegative O species,
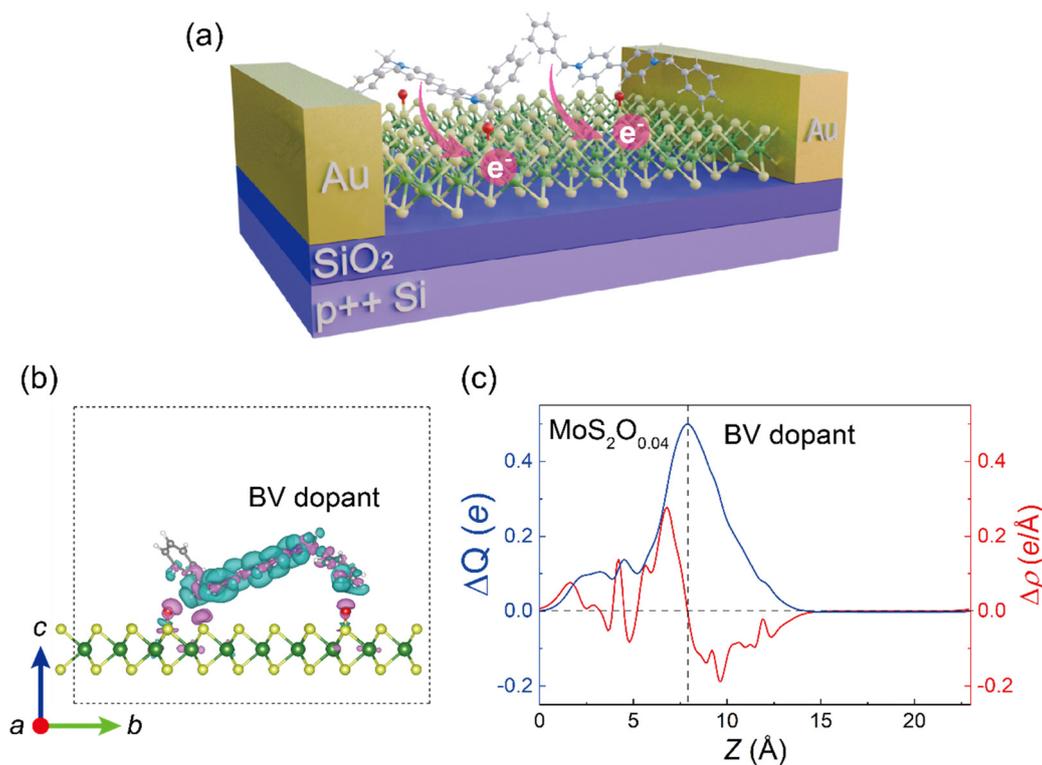


**Fig. 5** (a) Schematic of device setup of $MoS_2O_x$ FETs after surface BV doping. The monolayer $MoS_2O_{0.04}$ serves as a gate layer and contact with Au electrode. (b) Charge redistribution across BV/$MoS_2O_{0.04}$ interfaces by DFT-calculated differential charge density with an iso-surface of $7 \times 10^{-3}$ e. The charge accumulation and dissipation regions are represented by pink and cyan colors, respectively. (c) Planar-averaged differential charge density $\Delta\rho$ and transferred charge $\Delta Q$ along the out-of-plane direction ($c$ axis). The dashed black line in (c) is used as a guide to the eye.

this 2D MoS$_2$–O hybrid layer can act as a host for assembling with positively charged nanoclusters or particles.[37]

Finally, we demonstrate a proof-of-concept device based on the physicochemical properties of the MoS$_y$O$_x$ layer in this work. Fig. 5(a) shows the device structure of benzyl viologen molecule (BV)-doped MoS$_2$O$_x$ FETs with Au layer as contact metal. BV is a common n-type dopant with strong reductant ability for nanomaterials.[22,67,68] Fig. 5(b) shows the MoS$_2$O$_{0.04}$/BV interface model, where a BV molecule interacts with MoS$_2$O$_{0.04}$ through the stretched oxygen site, and it can be seen that the BV molecule loses electrons (cyan surface for electron loss) which transfer to the MoS$_2$O$_{0.04}$ side (pink surface for electron gain). To quantify the interaction between the surface O species and BV molecules, the planar-averaged differential charge density $\Delta\rho$ and transferred charge $\Delta Q$ are considered, defined as:

$$\Delta\rho = \rho_{\text{MoS}_2\text{O}_{0.04}/\text{BV}} - \rho_{\text{MoS}_2\text{O}_{0.04}} - \rho_{\text{BV}} \tag{1}$$

$$\Delta Q(z) = \int_0^z \Delta\rho(z)\text{d}z \tag{2}$$

where $\rho_{\text{MoS}_2\text{O}_{0.04}/\text{BV}}$, $\rho_{\text{MoS}_2\text{O}_{0.04}}$, and $\rho_{\text{BV}}$ are the planar-averaged charge density of the entire interface system, isolated MoS$_2$O$_{0.04}$ flake, and isolated BV molecule, respectively, and $z$ is the vertical distance from the bottom. In Fig. 5(c), the maximum $\Delta Q$ value of $\sim 0.5e$ at the vdWs gap denotes the transferred electrons from each BV molecule to MoS$_2$O$_{0.04}$. This large transfer value indicates the strong anchoring of BV molecules on the oxygen site (O$_{\text{Top}}$).

## Conclusions

To summarize, the ubiquitous presence of oxygen species in the environment and synthesis processes renders a high possibility of oxygen uptake in MoS$_2$ samples. Here based on DFT calculations, we reveal the energetics, forms, and effects of oxygen adsorbates and dopants in MoS$_2$. We identify the two most stable forms of oxygen, surface atomic adsorbate O$_{\text{Top}}$ and substituting oxygen O$_\text{S}$, both of which are electronically inert and free of in-gap dopant-induced states despite appreciable local strains around the dopants. These dopant states would occur through a dissociative mechanism of O$_2$ trapped at the V$_\text{S}$ overcoming an energy barrier of $\sim 1.2$ eV. We predict that the hole mass is more sensitive to the oxygen content than the electron mass, due to less hybridization of oxygen with CBM. Controlling the oxygen stoichiometry allows modulation of the work function up to $\sim 0.5$ eV, which is favorable for reducing the SBH and contact resistance with metal electrodes. Our study elucidates the mechanism for controlling oxygen dopants on the MoS$_2$ monolayer to achieve modulated carrier mass and work function, motivating further study of emerging optoelectronic devices based on 2D materials.

## Methods

The Vienna *ab initio* simulation package (VASP) with the projected augmented wave (PAW) potential is adopted for density functional theory (DFT) calculations.[69] Exchange and correlation energy of electrons are considered through the generalized gradient approximation (GGA) with the Perdew–Burke–Ernzerhof (PBE) functional.[70] The DFT-D2 method of Grimme is used to describe the vdWs interactions, this correction having been widely adopted for multiple low-dimensional materials.[71] The energy cutoff is set to 450 eV and sampling of the Brillouin zone is performed by using a uniform $3 \times 3 \times 1$ dense $k$-point grid. Energy and forces are converged until $10^{-5}$ eV and 0.01 eV Å$^{-1}$, respectively. A slab model is based on a $5 \times 5 \times 1$ supercell with a vacuum space with a thickness of 15 Å to avoid interactions from periodic replicas. The vacuum layer thickness is tested for the coverage of work function (see Fig. S11, ESI†). Spin polarization is considered in all calculations. The lattice constraint values are calculated by comparing the lattice constants of oxygen-adsorbed systems and those of the pristine MoS$_2$ monolayer. The chemical potential ($\mu$) should be considered for the formation of MoS$_2$ film. Here, the energy values based on DFT results are used for estimating the formation energy of O adsorbates on MoS$_2$ within the allowed crystal growth conditions with the chemical potential of sulfur species ($\mu_\text{s}$) varying from S-poor to S-rich conditions. The stability of these O adsorbates is estimated by judging $E_\text{f}$ defined as:

$$E_\text{f} = E(\text{O:MoS}_2) - E(\text{MoS}_2) - \sum_i n_i\mu_i \tag{3}$$

where $E(\text{O:MoS}_2)$ and $E(\text{MoS}_2)$ are the total energy of the O-adsorbed system and the equivalent MoS$_2$ supercell, respectively. The doped system is formed by either adding (positive) or removing (negative) $n_i$ atoms for the $i$ type of atom with a chemical potential of $\mu_i$, with $i$ being S (sulfur) or O (oxygen). By assuming the chemical potential of Mo and S are in thermal equilibrium with MoS$_2$, $\mu_{\text{Mo}}$ and $\mu_\text{s}$ satisfy the relation:

$$\mu_{\text{MoS}_2} = 2\mu_\text{s} + \mu_\text{O} \tag{4}$$

where $\mu_{\text{MoS}_2}$ represents total energy of MoS$_2$ per formula unit. For the S-rich limit condition, the source of sulfur is from gaseous S$_8$ molecules during chemical vapor growth; therefore S$_8$ is chosen as the reference state for determining $\mu_{\text{Mo,max}} = E_{\text{S}_8}$, where $E_{\text{S}_8}$ is the total energy of molecular crystal S$_8$ per atom obtained from DFT calculation. Under the Mo-rich limit (in the meanwhile S-poor limit) condition, $\mu_{\text{Mo,max}} = E_{\text{Mo}}$, and $E_{\text{Mo}}$ is the energy of bulk Mo bcc phase metal crystal per atom from DFT results, while $\mu_{\text{s,min}} = (\mu_{\text{MoS}_2} - \mu_{\text{Mo,max}})/2$ as required by the assumption of equilibrium-growth condition. The chemical potential of O atom ($\mu_\text{O}$) and O$_2$ molecule ($\mu_{\text{O}_2}$) are the energy of isolated O atom and O$_2$ molecule, respectively. Dipole correction is added for all structures along the out-of-plane direction to avoid deviation of the total energy, atomic forces, and electrostatic potential.[72] $W$ is extracted from the following formula:

$$W = E_{\text{vac}} - E_\text{F} \tag{5}$$

where $E_{\text{vac}}$ is the vacuum energy level and $E_\text{F}$ refers to the Fermi level. $W$ of metal electrodes are referred to experimental values.[73] The diffusion energy barriers for oxygen atom diffusion along certain paths over the MoS$_2$ surface are calculated though the CI-NEB method.[74] Part of data postprocessing is

conducted by the Vaspkit code, and Vesta software is used for atomic structure visualization.[75,76]

## Author contributions

Hejin Yan and Yongqing Cai: conceptualization, methodology, and writing – original draft. Hongfei Chen and Xiangyue Cui: software and validation. Qiye Guan: data curation and validation. Bowen Wang: visualization and investigation. Yongqing Cai: supervision. All authors participated in general discussion and manuscript revision.

## Data availability

All relevant data are available from the authors on reasonable request and/or are included within the article and the ESI.†

## Conflicts of interest

The authors declare that they have no conflict of interest.

## Acknowledgements

## References

1 A. Daus, S. Vaziri, V. Chen, Ç. Köroğlu, R. W. Grady, C. S. Bailey, H. R. Lee, K. Schauble, K. Brenner and E. Pop, *Nat. Electron.*, 2021, **4**, 495–501.

2 J. Tang, Q. Wang, J. Tian, X. Li, N. Li, Y. Peng, X. Li, Y. Zhao, C. He and S. Wu, *Nat. Commun.*, 2023, **14**, 3633.

3 A. Liu, X. Zhang, Z. Liu, Y. Li, X. Peng, X. Li, Y. Qin, C. Hu, Y. Qiu and H. Jiang, *Nano-Micro Lett.*, 2024, **16**, 119.

4 S. Das, A. Sebastian, E. Pop, C. J. McClellan, A. D. Franklin, T. Grasser, T. Knobloch, Y. Illarionov, A. V. Penumatcha and J. Appenzeller, *Nat. Electron.*, 2021, **4**, 786–799.

5 Y. Zou, P. Li, C. Su, J. Yan, H. Zhao, Z. Zhang and Z. You, *ACS Nano*, 2024, **18**, 9627–9635.

6 S. Aftab, M. Z. Iqbal, S. Hussain, H. H. Hegazy, F. Kabir, S. H. A. Jaffery and G. Koyyada, *Chem. Eng. J.*, 2023, 144039.

7 Y. Kim, I. Sohn, D. Shin, J. Yoo, S. Lee, H. Yoon, J. Park, S.-M. Chung and H. Kim, *Adv. Eng. Mater.*, 2024, **26**, 2301063.

8 D. Panchal, A. Sharma and S. Pal, *Mater. Today Sustain.*, 2023, **21**, 100264.

9 T. Wu, Y. Song, Z. Shi, D. Liu, S. Chen, C. Xiong and Q. Yang, *Nano Energy*, 2021, **80**, 105541.

10 D. Guo, X.-x Xue, M. Jiao, J. Liu, T. Wu, X. Ma, D. Lu, R. Zhang, S. Zhang, G. Shao and Z. Zhou, *Chem. Sci.*, 2024, **15**, 16281–16290.

11 G. Shao, J. Xu, S. Gao, Z. Zhang, S. Liu, X. Zhang and Z. Zhou, *Carbon Energy*, 2024, **6**, e417.

12 X. Huang, C. Liu and P. Zhou, *npj 2D Mater. Appl.*, 2022, **6**, 51.

13 S. Aftab, H. H. Hegazy and F. Kabir, *Adv. Mater. Technol.*, 2023, **8**, 2201897.

14 Y. Jing, X. Tan, Z. Zhou and P. Shen, *J. Mater. Chem. A*, 2014, **2**, 16892–16897.

15 B. Radisavljevic and A. Kis, *Nat. Mater.*, 2013, **12**, 815–820.

16 Y. Shen, Z. Dong, Y. Sun, H. Guo, F. Wu, X. Li, J. Tang, J. Liu, X. Wu and H. Tian, *Adv. Mater.*, 2022, **34**, 2201916.

17 F. Wu, H. Tian, Y. Shen, Z. Hou, J. Ren, G. Gou, Y. Sun, Y. Yang and T.-L. Ren, *Nature*, 2022, **603**, 259–264.

18 J. Xu, L. Chen, Y.-W. Dai, Q. Cao, Q.-Q. Sun, S.-J. Ding, H. Zhu and D. W. Zhang, *Sci. Adv.*, 2017, **3**, e1602246.

19 K. Santosh, R. C. Longo, R. Addou, R. M. Wallace and K. Cho, *Nanotechnology*, 2014, **25**, 375703.

20 J. Hong, Z. Hu, M. Probert, K. Li, D. Lv, X. Yang, L. Gu, N. Mao, Q. Feng and L. Xie, *Nat. Commun.*, 2015, **6**, 6293.

21 C. Kim, I. Moon, D. Lee, M. S. Choi, F. Ahmed, S. Nam, Y. Cho, H.-J. Shin, S. Park and W. J. Yoo, *ACS Nano*, 2017, **11**, 1588–1596.

22 J. Jang, J.-K. Kim, J. Shin, J. Kim, K.-Y. Baek, J. Park, S. Park, Y. D. Kim, S. S. Parkin and K. Kang, *Sci. Adv.*, 2022, **8**, eabn3181.

23 M. Yarali, Y. Zhong, S. N. Reed, J. Wang, K. A. Ulman, D. J. Charboneau, J. B. Curley, D. J. Hynek, J. V. Pondick and S. Yazdani, *Adv. Electron. Mater.*, 2021, **7**, 2000873.

24 E. Mitterreiter, B. Schuler, A. Micevic, D. Hernangómez-Pérez, K. Barthelmi, K. A. Cochrane, J. Kiemle, F. Sigger, J. Klein and E. Wong, *Nat. Commun.*, 2021, **12**, 3822.

25 X. Zhang, Z. Shao, X. Zhang, Y. He and J. Jie, *Adv. Mater.*, 2016, **28**, 10409–10442.

26 H. Liu, M. Si, S. Najmaei, A. T. Neal, Y. Du, P. M. Ajayan, J. Lou and P. D. Ye, *Nano Lett.*, 2013, **13**, 2640–2646.

27 Y.-H. Lee, X.-Q. Zhang, W. Zhang, M.-T. Chang, C.-T. Lin, K.-D. Chang, Y.-C. Yu, J. T.-W. Wang, C.-S. Chang and L.-J. Li, *Adv. Mater.*, 2012, **24**, 2320–2325.

28 J. V. Pondick, J. M. Woods, J. Xing, Y. Zhou and J. J. Cha, *ACS Appl. Nano Mater.*, 2018, **1**, 5655–5661.

29 X. Wang, H. Feng, Y. Wu and L. Jiao, *J. Am. Chem. Soc.*, 2013, **135**, 5304–5307.

30 Y.-H. Lee, L. Yu, H. Wang, W. Fang, X. Ling, Y. Shi, C.-T. Lin, J.-K. Huang, M.-T. Chang and C.-S. Chang, *Nano Lett.*, 2013, **13**, 1852–1857.

31 J.-K. Huang, Y. Wan, J. Shi, J. Zhang, Z. Wang, W. Wang, N. Yang, Y. Liu, C.-H. Lin and X. Guan, *Nature*, 2022, **605**, 262–267.

32 Y. Y. Illarionov, T. Knobloch, M. Jech, M. Lanza, D. Akinwande, M. I. Vexler, T. Mueller, M. C. Lemme, G. Fiori and F. Schwierz, *Nat. Commun.*, 2020, **11**, 3385.

33 C. Zhang, T. Tu, J. Wang, Y. Zhu, C. Tan, L. Chen, M. Wu, R. Zhu, Y. Liu and H. Fu, *Nat. Mater.*, 2023, **22**, 832–837.

34 Y. Jin, J. Sun, L. Zhang, J. Yang, Y. Wu, B. You, X. Liu, K. Leng and S. Liu, *Adv. Mater.*, 2023, **35**, 2212079.

35 Y. Jiang, Z. Liu, H. Zhou, A. Sharma, J. Deng and C. Ke, *Nanotechnology*, 2023, **34**, 405701.

36 M. M. Perera, M.-W. Lin, H.-J. Chuang, B. P. Chamlagain, C. Wang, X. Tan, M. M.-C. Cheng, D. Tománek and Z. Zhou, *ACS Nano*, 2013, **7**, 4449–4458.

37 S. Kc, R. C. Longo, R. M. Wallace and K. Cho, *J. Appl. Phys.*, 2015, **117**, 135301.

38 S. Wang, X. Zeng, Y. Zhou, J. Lu, Y. Hu, W. Wang, J. Wang, Y. Xiao, X. Wang and D. Chen, *ACS Appl. Electron. Mater.*, 2022, **4**, 955–963.

39 H. Nam, S. Wi, H. Rokni, M. Chen, G. Priessnitz, W. Lu and X. Liang, *ACS Nano*, 2013, **7**, 5870–5881.

40 Y. A. Kabachii, A. S. Golub, S. Y. Kochev, N. D. Lenenko, S. S. Abramchuk, M. Y. Antipin, P. M. Valetsky, B. D. Stein, W. E. Mahmoud and A. A. Al-Ghamdi, *Chem. Mater.*, 2013, **25**, 2434–2440.

41 L. Wang, Z. Chen, C. R. Dean, T. Taniguchi, K. Watanabe, L. E. Brus and J. Hone, *ACS Nano*, 2012, **6**, 9314–9319.

42 Q. He, Z. Zeng, Z. Yin, H. Li, S. Wu, X. Huang and H. Zhang, *Small*, 2012, **8**, 2994–2999.

43 P.-C. Shen, Y. Lin, C. Su, C. McGahan, A.-Y. Lu, X. Ji, X. Wang, H. Wang, N. Mao and Y. Guo, *Nat. Electron.*, 2022, **5**, 28–36.

44 I. Lee, M. Kang, S. Park, C. Park, H. Lee, S. Bae, H. Lim, S. Kim, W. Hong and S. Y. Choi, *Small*, 2024, **20**, 2305143.

45 H. Shin, Y. Luo, A. Benali and Y. Kwon, *Phys. Rev. B*, 2019, **100**, 075430.

46 A. Soman, R. A. Burke, Q. Li, M. D. Valentin, T. Li, D. Mao, M. Dubey and T. Gu, *ACS Appl. Mater. Interfaces*, 2020, **12**, 37305–37312.

47 B. H. Kim, M. Park, M. Lee, S. J. Baek, H. Y. Jeong, M. Choi, S. J. Chang, W. G. Hong, T. K. Kim and H. R. Moon, *RSC Adv.*, 2013, **3**, 18424–18429.

48 T. Jurca, M. J. Moody, A. Henning, J. D. Emery, B. Wang, J. M. Tan, T. L. Lohr, L. J. Lauhon and T. J. Marks, *Angew. Chem., Int. Ed.*, 2017, **56**, 4991–4995.

49 C. Ataca and S. Ciraci, *Phys. Rev. B: Condens. Matter Mater. Phys.*, 2012, **85**, 195410.

50 F.-X. R. Chen, N. Kawakami, C.-T. Lee, P.-Y. Shih, Z.-C. Wu, Y.-C. Yang, H.-W. Tu, W.-B. Jian, C. Hu and C.-L. Lin, *Appl. Phys. Lett.*, 2022, **121**, 151601.

51 K. Burns, A. M. Z. Tan, H. Gordon, T. Wang, A. Gabriel, L. Shao, R. G. Hennig and A. Aitkaliyeva, *Phys. Rev. B*, 2020, **102**, 085421.

52 K. S. Kumar, A. K. Dash, H. Sabreen H, M. Verma, V. Kumar, K. Watanabe, T. Taniguchi, G. S. Gautam and A. Singh, *2D Mater.*, 2024, **12**, 045003.

53 A. Nourbakhsh, M. Cantoro, T. Vosch, G. Pourtois, F. Clemente, M. H. Van Der Veen, J. Hofkens, M. M. Heyns, S. De Gendt and B. F. Sels, *Nanotechnology*, 2010, **21**, 435203.

54 Y. Cai, G. Zhang and Y.-W. Zhang, *J. Am. Chem. Soc.*, 2014, **136**, 6269–6275.

55 B. Hou, Y. Zhang, H. Zhang, H. Shao, C. Ma, X. Zhang, Y. Chen, K. Xu, G. Ni and H. Zhu, *J. Phys. Chem. Lett.*, 2020, **11**, 3116–3128.

56 Z. Wei, J. Tang, X. Li, Z. Chi, Y. Wang, Q. Wang, B. Han, N. Li, B. Huang and J. Li, *Small Methods*, 2021, **5**, 2100091.

57 J. Tang, Z. Wei, Q. Wang, Y. Wang, B. Han, X. Li, B. Huang, M. Liao, J. Liu and N. Li, *Small*, 2020, **16**, 2004276.

58 X. Zheng, A. Calò, E. Albisetti, X. Liu, A. S. M. Alharbi, G. Arefe, X. Liu, M. Spieser, W. J. Yoo and T. Taniguchi, *Nat. Electron.*, 2019, **2**, 17–25.

59 X. Liu, M. S. Choi, E. Hwang, W. J. Yoo and J. Sun, *Adv. Mater.*, 2022, **34**, 2108425.

60 X. Tong, E. Ashalley, F. Lin, H. Li and Z. M. Wang, *Nano-Micro Lett.*, 2015, **7**, 203–218.

61 H. Gao, M. Hu, J. Ding, B. Xia, G. Yuan, H. Sun, Q. Xu, S. Zhao, Y. Jiang and H. Wu, *Adv. Funct. Mater.*, 2023, **33**, 2213410.

62 Q. Guan, H. Yan and Y. Cai, *Adv. Mater. Interfaces*, 2022, **9**, 2101838.

63 S. Gupta, A. Johnston and S. Khondaker, *J. Appl. Phys.*, 2022, **131**, 164303.

64 A. Oberoi, Y. Han, S. P. Stepanoff, A. Pannone, Y. Sun, Y.-C. Lin, C. Chen, J. R. Shallenberger, D. Zhou and M. Terrones, *ACS Nano*, 2023, **17**, 19709–19723.

65 S. Das, H.-Y. Chen, A. V. Penumatcha and J. Appenzeller, *Nano Lett.*, 2013, **13**, 100–105.

66 S. Nagarajan, D. Hiller, I. Ratschinski, D. König, S. C. Smith, T. Mikolajick and J. Trommer, *Adv. Mater. Interfaces*, 2024, **11**, 2300600.

67 D. Kiriya, M. Tosun, P. Zhao, J. S. Kang and A. Javey, *J. Am. Chem. Soc.*, 2014, **136**, 7853–7856.

68 X. Tong, E. Ashalley, F. Lin, H. Li and Z. M. Wang, *Nano-Micro Lett.*, 2015, **7**, 203–218.

69 G. Kresse and J. Furthmüller, *Comput. Mater. Sci.*, 1996, **6**, 15–50.

70 G. Kresse and D. Joubert, *Phys. Rev. B: Condens. Matter Mater. Phys.*, 1999, **59**, 1758.

71 S. Grimme, *J. Comput. Chem.*, 2006, **27**, 1787–1799.

72 L. Bengtsson, *Phys. Rev. B: Condens. Matter Mater. Phys.*, 1999, **59**, 12301.

73 W. M. Haynes, *CRC handbook of chemistry and physics*, CRC press, 2016.

74 G. Henkelman, B. P. Uberuaga and H. Jónsson, *J. Chem. Phys.*, 2000, **113**, 9901–9904.

75 V. Wang, N. Xu, J.-C. Liu, G. Tang and W.-T. Geng, *Comput. Phys. Commun.*, 2021, **267**, 108033.

76 K. Momma and F. Izumi, *J. Appl. Crystallogr.*, 2008, **41**, 653–658.